Abram, Rafal; Chrobak, Dariusz; Byggmästar, Jesper; Nordlund, Kai; Nowak, Roman

Comprehensive structural changes in nanoscale-deformed silicon modelled with an integrated atomic potential

Published in:
Materialia

DOI:
10.1016/j.mtla.2023.101761

Published: 01/05/2023

Document Version
Publisher's PDF, also known as Version of record

Please cite the original version:
Abram, R., Chrobak, D., Byggmästar, J., Nordlund, K., & Nowak, R. (2023). Comprehensive structural changes in nanoscale-deformed silicon modelled with an integrated atomic potential. *Materialia*, *28*, Article 101761. https://doi.org/10.1016/j.mtla.2023.101761

MTLA 28 (2023) 101761

Contents lists available at ScienceDirect

Materialia

journal homepage: www.elsevier.com/locate/mtla

Comprehensive structural changes in nanoscale-deformed silicon modelled with an integrated atomic potential

Rafal Abram[a,1], Dariusz Chrobak[b,1], Jesper Byggmästar[c], Kai Nordlund[c], Roman Nowak[a,d,1,*]

[a] Nordic Hysitron Laboratory, Department of Chemistry and Materials Science, School of Chemical Engineering, Aalto University, Aalto 00076, Finland
[b] Institute of Materials Engineering, University of Silesia in Katowice, 75 Pułku Piechoty 1, Chorzów 41-500, Poland
[c] Department of Physics, University of Helsinki, P.O. Box 43, FI-00014, Finland
[d] Division of Materials Chemistry, Faculty of Engineering, Hokkaido University, Sapporo 060-8628, Japan

ARTICLE INFO

Keywords:
Silicon
Nanoscale surface deformation
Molecular dynamics simulations
Phase transformations
Dislocations

ABSTRACT

In spite of remarkable developments in the field of advanced materials, silicon remains one of the foremost semiconductors of the day. Of enduring relevance to science and technology is silicon's nanomechanical behaviour including phase transformation, amorphization and dislocations generation, particularly in the context of molecular dynamics and materials research. So far, comprehensive modelling of the whole cycle of events in silicon during nanoscale deformation has not been possible, however, due to the limitations inherent in the existing interatomic potentials. This paper examines how well an unconventional combination of two well-known potentials - the Tersoff and Stillinger-Weber - can perform in simulating that complexity. Our model indicates that an irreversible deformation of silicon (Si-I) is set in motion by a transformation to a non-diamond structure (Si-nd), and followed by a subsequent transition to the Si-II and Si-XII phases (Si-1→Si-nd→Si-II→Si-XII). This leads to the generation of dislocations spreading outwards from the incubation zone. In effect, our simulations parallel the structural changes detected experimentally in the deformed material. This includes both the experimentally observed sequence of phase transitions and dislocation activity, which - taken together - neither the Tersoff nor Stillinger-Weber, or indeed any other available Si interatomic potential, is able to achieve in its own right. Notably, the Si-XII phase was not discerned by any of the previous computational models, which points towards the effectiveness of our integrated approach to forecasting novel phenomena discovered by advanced structure examinations. Last not least, our method satisfies the demand for a quick means to construct potentials by opening up the huge library of existing models to new applications in various branches of materials science.

1. Introduction

1.1. *Mechanical behaviour of silicon*

Silicon is a material with a superior blend of physical properties and well-established means of fabrication, finding application in a vast range of fields [1] from electronics and photonics to micro-and nano-electromechanical systems, to name but a few. Early research into silicon discovered its exceptional mechanical properties, and has been widely published [2]. In particular, pioneering hardness experiments by Giardini [3], Gerk and Tabor [4], Petersen [5] as well as Gilman [6,7] revealed silicon's unorthodox mechanical behaviour. The mechanical response of silicon differed from that of other materials by having its plastic deformation rely on pressure-induced transformation from a diamond (Si-I) to β-tin (Si-II) structure [4,6,7], accompanied by dislocation mechanisms characteristic of crystalline solids (*e.g.*, [6]). This has led to a close investigation of stress-induced metallization and amorphization of an indented Si-crystal [8].

With the advent of depth-sensing nanoindentation technology [9–11], hardness experiments on silicon reached a new level. Early results by Pethica *et al.* [11] and Pharr *et al.* [12] and a rapid development of the nanoindentation method led to the recognition of the complexity of silicon nanodeformation, by contrast with other ceramics or metallic crystals [13–15]. Research into the role of phase transformations in

---

* Corresponding author at: Nordic Hysitron Laboratory, Department of Chemistry and Materials Science, School of Chemical Engineering, Aalto University, Aalto 00076, Finland

E-mail address: roman.nowak@aalto.fi (R. Nowak).

[1] These authors equally contributed to the present work

https://doi.org/10.1016/j.mtla.2023.101761
Received 17 December 2022; Accepted 28 March 2023

nanodeformed silicon has continued (*e.g.*, [15–19]), and it seems far from having reached its saturation point (see *e.g.*, [18–26]), being increasingly supported by atomistic modelling [27–31].

1.2. Atomistic simulations

Modern materials science owes much of its success to computer simulations [32], which examine and predict a large array of phenomena (*e.g.*, [24–30]). The molecular dynamics (MD) simulation method accounts for the interatomic forces in terms of the gradient of the potential energy function in conjunction with a set of adjustable parameters to predict the specific conduct of a modelled system. Inevitably, whether or not the outcome of simulation reflects a given set of experimental data depends on the adopted interatomic interaction model [32, 33]. Materials physics has no shortage of "ready-made" potentials at its disposal, however, their limited transferability means that one process is usually modelled at the expense of another, thus precluding the interplay of key phenomena. Indeed, any model of atomic interactions involves a trade-off between accuracy, adaptability and computational resources [32]. Thus, a careful consideration of the available interatomic potentials focusing transferability precedes any MD simulations [34,35].

Often, after deciding that none of the applied potentials mirrors a system's behaviour of interest, developing a suitable one 'from scratch' becomes a necessity. It is a complex and time-consuming trial and error process. Here we examine a simple and promising alternative: it is to merge two already existing - yet operationally diverse – potentials developed for Si crystal, into a single one. This new, integrated potential (IP) - by combining the unique characteristics of its components - makes it possible to simulate some crucial, coexisting features of a system under examination. Using the IP-approach, we have been able to deal with the intricate process of nanoindentation deformation of silicon in a more satisfactory way than appears possible with the currently available potentials [32,33].

1.3. Structure evolution in nanodeformed Si

As already mentioned, silicon is probably the most extensively studied semiconductor in modern technology. Its applications include surface acoustic wave photonic devices [36], light sources [37] or atomic scale instruments and memories [38]. One can therefore be forgiven for believing that every property of this important material has been thoroughly investigated [39]. But the fact of the matter is that such phenomena as nanoscale deformation of silicon crystal, and its incipient plasticity, in particular, are far from being fully understood. Numerous nanoindentation experiments, combined with microscopic observations, demonstrate that, under increasing straining, the initial Si-I structure undergoes a series of transformations to high-pressure Si-II phase. The latter converts during the unloading to the Si-III/Si-XII combination and amorphous Si phases [22,40–47]. This, however, is not the complete picture as it disregards the presence of dislocations, slip bands, and cracks in the vicinity of the acting indenter tip [17,20,22,45,48]. A microscopic examination by Wong *et al.* [22,43–46] of the Si structure developed under a spherical indenter led them to the conclusion that phase transformation and defects generation were "competing deformation mechanisms, with one or the other process initiating plastic deformation under particular loading conditions". Similarly, nanoindentation-induced elastic-plastic transition in GaAs crystal is initiated by a phase transformation [49–51], while nanoscale plasticity in GaN is exclusively governed by dislocations [52,53].

What we are dealing with here are two distinct mechanisms of silicon's incipient plasticity: in the first, phase transformation assumes the dominant role followed by dislocation activity, while in the second, plasticity starts with the nucleation of defects. Regardless of which scenario unfolds in practice, none of the currently available potentials meets the requirement of accurately modelling a complex nanoindentation process, since each one of them suffers either from limited transferability [54] or high computational-time expense. Such is the case with the interatomic potentials developed with the aid of machine learning [55,56] which are capable of a high degree of accuracy, even on a par with ab initio methods. However, they frequently exhibit such computational complexity as to render them impracticable for the purpose of nanoindentation, which requires a simultaneous consideration of multimillion atomic systems and the application of long-time scales [33]. As a result, modelling silicon mechanical behaviour continues to rely heavily on either the Stillinger-Weber (SW) [57] or Tersoff-type [58–65] potentials. The former has been designed with the Si-I and amorphous phase in mind, proving particularly efficient at capturing dislocation-based processes. By contrast, Tersoff-type potentials reflect phase transformations that occur in the high-pressure phases (diamond cubic and metallic) of silicon. It follows that neither model is versatile enough to accurately reflect the interplay between both phenomena, thus precluding proper investigation of Si crystal behaviour under localized stress.

An early critical appraisal of the interatomic potentials for Si has been published by Balamane *et al.* [66], while tests on the Si lattice under large shear strain have been performed by Godet *et al.* [67]. Furthermore, there have been numerous efforts to modify the original Tersoff interatomic potential (*e.g.* [62]) in order to increase its accuracy and transferability. Kumagai *et al.* [64] revised the angular-dependent term of the Tersoff formula, considerably improving the description of silicon's elastic properties as well as melting temperature. In consequence, the Kumagai's potential has recently been employed to model nanoindentation-induced deformation of silicon [68,69]. The most significant advance in the simulation of silicon brittle behaviour has been achieved by Pastewka *et al.* [36], whose screened version of the Tersoff-type potential manages to capture both phase transformations and dislocation activity in silicon [70–72]. Even the most advanced, this interatomic potential - when applied to nanoscale indentation - results in an overestimation of contact pressure at the onset of phase transformation, as well insufficiently developed dislocation structure [71]. The overall conclusion is that crystalline phase transformations in silicon are usually modelled at the expense of dislocation movements, or vice versa [47,73] and a more adaptable interatomic potential is required.

To recapitulate, the integrated interatomic potential (IP) of our design, obtained by simply merging the Tersoff [59] and Stillinger-Weber [57] models, appears well-suited to MD-modelling of the structural changes in nanodeformed Si-crystal, proving it inherits the essential features of the component potentials. Our results provide a consistent account of the sequence of phase transformations and dislocation activity, both of which play a crucial role in nanoindentation-induced plasticity of silicon. Finally, our findings concerning the structure evolution in a stressed nano-volume of silicon — by virtue of being firmly rooted in MD simulations - are in line with the recent research into silicon, whether dealing with the structure and stability of the interstitial defects [74], the amorphization by mechanical deformation [75,76], shuffle dislocations motion in Si-crystals [25, 77] or low-temperature undissociated-dislocations-mediated plasticity [31].

2. Computational

2.1. The integrated potential for Si

Our own experience [47,73] and that of other authors (*e.g.*, [78]) shows that satisfactory modelling of Si behaviour exclusively with the Tersoff (T2) potential [59] is limited to phase-transformation governed phenomena. A similar problem arises with the SW potential [57], whose competence is limited to deformation processes steered by dislocation-activity [73]. Faced with this dilemma, we have attempted to merge the Stillinger-Weber and Tersoff potentials - two of the most acclaimed interatomic potentials for silicon - into a single model in order to obtain one of enhanced transferability.

The solution we offer consists of the integrated potential (IP), based on a weighted sum of the SW and T2 (Tersoff) potentials, such that the potential energy $E_{IP} = w_{T2}E_{T2} + w_{SW}E_{SW}$, where the weights comply the relationship: $w_{T2} + w_{SW} = 1$, and E_{T2} and E_{SW} stand for potential energy of the T2 [59] and SW [57] interaction model, respectively. Careful testing of various versions of our integrated potential resulted in a unique IP-combination with the weight values $w_{T2} = 0.71875$ and $w_{SW} = 0.28125$, which we regard as close to optimal for silicon under localized stress (Supplementary Note 1). Although the mathematical forms of the T2 and SW potentials differ, each one can be viewed as an angle-dependent EAM (Embedded Atom Method) potential [79]. The purpose of complementing the T2 model with a smaller share of the SW potential was to "stiffen" the response of the former. It needs reminding that the SW potential contains a penalty function strongly suppressing deviation from the bond angle of 109.47°, characteristics of diamond structure. Details of the proposed integrated IP potential and its application with the MD simulation package (LAMMPS [80]) are provided in the Supplementary Note 1.

2.2. *Initial testing of integrated IP potential for Si*

Initial testing of IP performance in simulating silicon was carried out using the T2 and SW potentials, alongside the screened T3s model [36], for comparison. It concerned potential energy *E(r)* and its derivative (*dE/dr*) calculated as the function of the interatomic distance *r* in the Si-Si dimer, followed by an evaluation of the elastic constants, cohesion energy, formation energy of native point defects and the generalized stacking fault energy (GSFE) curve for the glide <112> {111} slip system. The cohesion energy was defined as a ratio of the total potential energy and the number of atoms, while the elastic constants were estimated by applying small volumetric, tetragonal and rhombohedral deformations to the Si unit cell. Furthermore, we were able to evaluate the formation energy of vacancies (V) as well as hexagonal (I_H), tetragonal (I_T) and split $I_{<110>}$ interstitials, while the GFSE-curve calculations followed these introduced by Branicio *et al.* [81]. The computations were accomplished with the LAMMPS simulation package [80], while the calculations with the screened T3s potential required the employment of a code from the library of interatomic potentials ATOMISTICA [82]. They (except GSFE) involved a supercell of the Si-I phase (4096 atoms) composed of 8 × 8 × 8 Si unit cells with the initial lattice parameter of a=5.431 Å. The final adjustment of atomic positions was achieved using the conjugate gradient method.

Our initial results prove that the IP potential inherits the characteristics of both the T2 and SW potentials, as well as showing considerable promise for modelling the structural changes in silicon under complex stress. It is worth noting that the energy curve of the Si-Si dimer (Fig. 1a) obtained with the IP potential (red) is located in-between those obtained with the T2 (green) and SW models (black), its exact position depending on the combination of the w_{T2} and w_{SW} parameters. On the other hand, we found the IP simulation delivered a marginally lower Si-Si dimer's binding energy than the T3s (Fig. 1a). It was also characterised by a smaller range, leading to a shorter simulation time. The decrease in the force-barrier of the Si-Si dimer (Fig. 1b) suggests the IP has retained the attributes of the T2 potential in addition to its increased ability to describe dislocation activity.

Further comparative examinations of the IP, T2, SW and T3s interatomic potentials' performance, when applied to silicon, include the elastic constants (c_{11}, c_{12}, c_{44}), cohesive energy (E_c), unstable stacking fault ($E_{<112>}$) and point defects formation ($I_{<110>}$, I_H, I_T) energies, whose values have been listed in Table 1.

It seems quite remarkable that the results obtained with IP are close to the weighted sum value of those calculated with the T2 and SW potentials, a minor exception being the c_{44} elastic constant. It is also worth noting that the results of our simulations with the aid of IP-potential concerning point-defects in silicon agree with the data presented by other authors (refer to Table 1). Moderate deviation has been detected only in the case of the I_H self-interstitial, exceeding the upper limit of I_H-energy of 0.78 eV provided by Holmström *et al.* [84]. In contrast to the hexagonal interstitial, the split $I_{<110>}$ point defect appears to have the most stable constitution also according to our calculations with integrated IP potential (Table 1), thus in line with the quantum Monte Carlo simulations [85]. Furthermore, simulations with the screened T3s potential provide the lowest formation energy of the tetragonal I_T self-interstitial, which appears to contradict other published data (refer

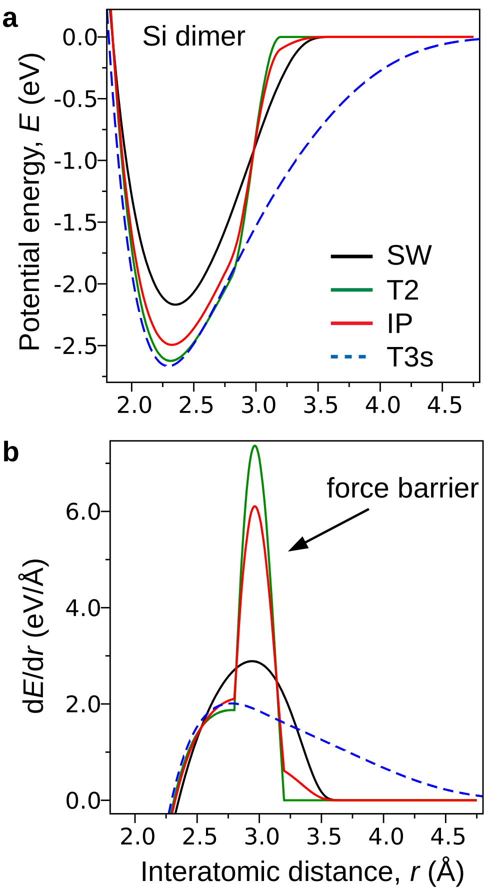

Fig. 1. The potential energy *E(r)* of a two-body interaction between the atoms of the Si-Si dimer determined with the IP (red), SW (black), T2 (green) and T3s (blue) potentials (a) and its derivative *dE/dr* functions (b).

Table 1
Cohesive energy E_c (eV), elastic constants c_{ij} (GPa), relaxed stacking fault energy $E_{<112>}$ (J/m^2), vacancy V and self-interstitials ($I_{<110>}$, I_H, I_T) energy formation (eV) calculated with the T2, SW, IP and T3s potentials. The lattice constant of the Si-I phase is 5.431 Å, regardless of the potential selection. The weighted sum $w_1X_1 + w_2X_2$ of the considered silicon properties is also displayed.

	T2 X_1	SW X_2	$w_1X_1+w_2X_2$	IP	T3s	Published data
E_c	-4.63	-4.34	-4.55	-4.55	-4.63	-4.62 [65]
c_{11}	122	151	130	130	143	166 [65]
c_{12}	86	76	83	83	75	64 [65]
c_{44}	10	57	23	24	69	80 [65]
						1.91 [67]
$E_{<112>}$	1.84	3.20	2.22	2.22	2.20	2.56 [83]
V	2.81	4.34	3.58	3.24	3.49	3.17-3.65 [84]
$I_{<110>}$	4.15	4.38	4.27	3.98	4.50	2.88-3.84 [84]
I_H	3.50	4.93	4.22	4.58	4.92	2.87-3.80 [84]
I_T	5.03	4.93	4.98	4.72	3.11	3.43-5.1 [84]

to Table 1).

As far as generalized stacking fault energy (GSFE) calculations are concerned, these were carried out using the supercell of the Si-I phase (diamond cubic structure) with the orientation defined by the low-index crystallographic directions $x[1\bar{1}0]$, $y[11\bar{2}]$, $z[111]$, as depicted in Fig. 2a. The modelled Si-crystal was composed of 30 atomic layers stacked on top of each other along the z[111] direction, with approximately 6Å thick vacuum sheet on top of the outer surface of the modelled material. The upper part of the silicon crystal (15 atomic layers) was displaced from its original position to a distance of $a/\sqrt{6}$ (a stands for the Si-I lattice parameter). The process was accomplished along the $y[11\bar{2}]$ direction in 200 consecutive steps. We optimized the x and z coordinates of the supercell after each step in such a way as to achieve its lowest potential energy. In this way, originally faultless silicon crystal was converted into one containing an intrinsic stacking fault (ISF), and the GSFE energy was derived from the equation: $E(b) = [E(b) - E_0]/A$, where E_0 defines the total energy of the perfect supercell, $E(b)$ stands for energy of the deformed supercell that involves the b displacement, and A is the glide plane area (details in Fig. 2b).

The unstable stacking fault (USF) energy can be easily deduced from the GSFE curves (Fig. 2b), as their maxima provide the requested values, equalling 3.16, 1.81, 2.19 and 2.19 J/m^2 for SW, T2, T3s and IP potentials. It is worth noting that the result obtained with our IP potential approaches the estimation available in the literature (cf. 1.91 J/m^2 [67], 1.95 J/m^2 [55], or 2.56 J/m^2 [83]). Moreover, the ISF values - defined as the final point (number 200) in each GSFE-curve - are as follows: 0.4, 0.8, 2.3 and 1.2 mJ/m^2 for SW, T2, T3s and IP, respectively. A comparison of the above with the value of 2 mJ/m^2, obtained using the GAP potential (Gaussian approximation potential framework [55]), leads inevitably to the conclusion that the T3s and IP models reproduce the USF energy more accurately than the SW and T2 approaches. It should be emphasized that we found the level of USF activation barrier of the <112>{111} slip in Si (Fig. 2b) to be a very useful characteristic serving as criterion for selecting the interatomic potential capable to model dislocation processes.

In summary, an initial examination of the IP model, alongside the T2, SW and T3s potentials suggests that our approach - although deceptively straightforward - shows considerable promise in capturing the structural changes occurring under complex stress. At the same time, it has to be admitted that the screened Tersoff T3s potential tends to provide a more accurate reflection of the elastic properties of Si than the IP model of our design.

2.3. MD-simulation of indentation in Si

The initial testing of the integrated IP potential was followed by 3-way MD-simulations of the spherical nanoindentation of the Si crystal in order to find out which of the employed potentials - IP, T2 or T3s - best reflected the structural changes known to occur under experimental conditions [20,22,40–46,48,73]. Excluded from the simulations was the SW potential, which does not capture pressure-induced transitions to crystalline phases of silicon [73].

MD simulations were performed with the LAMMPS simulation code for a silicon cluster (30.7 nm × 30.7 nm × 27.2 nm, 1328142 atoms) whose (001) surface was deformed under contact with a rigid, spherical diamond tip (radius of $R = 16.3$ nm). The coordination axes (X, Y, Z) were aligned along the [110], [-110] and [001] Si crystal directions respectively. Furthermore, the standard velocity-Verlet time integration scheme, with a time-step of 2 fs, was used throughout, while the Nose-Hoover thermostat was employed to control the system. Prior to running nanoindentation simulations, the system was relaxed to a thermal equilibrium at a target temperature of 300 K. Interactions between the diamond indenter tip and silicon crystal were modelled using the repulsive term of the Buckingham potential (the cut-off radius of 4 Å). MD-simulated nanoindentation of the Si crystal was accomplished by a sequence of tip displacements, with an increment of 0.5 Å every 15 ps, thus securing a quasi-static crystal deformation.

The defected structure generated in the deformed Si crystal was examined in detail using tools (modifiers) incorporated into the OVITO software [86,87]. In order to obtain a clear presentation of the structural changes in the Si crystal caused by nanoindentation, atoms belonging to the diamond structure have been disregarded. The applied procedure (Identify diamond structure modifier) leaves only atoms whose arrangement corresponds to the non-diamond (high-pressure) phases of silicon. Basic crystallographic data of selected silicon polytypes are presented in the Table S1. Moreover, the atoms have been attributed by the values of the shear strain (Atomic strain modifier). The identification of dislocations and their Burger's vectors was accomplished using the dislocation extraction algorithm (DXA modifier) [88].

We verified our findings in multiple ways, such as a visualization of the structural changes in nanoindented silicon, or by employing the bond-angle distribution (BADF) and radial distribution functions (RDF) to identify high-pressure silicon phases. The BADF was calculated by determining the bond angles in spheres with a radius 3 Å, centred on each Si atom. The range of bonding angles, 0°-180°, was divided into 200 sections. Then the number of bond angles N_i (i = 1, ...,200) belonging to the specific i-th interval was calculated. As the groups of

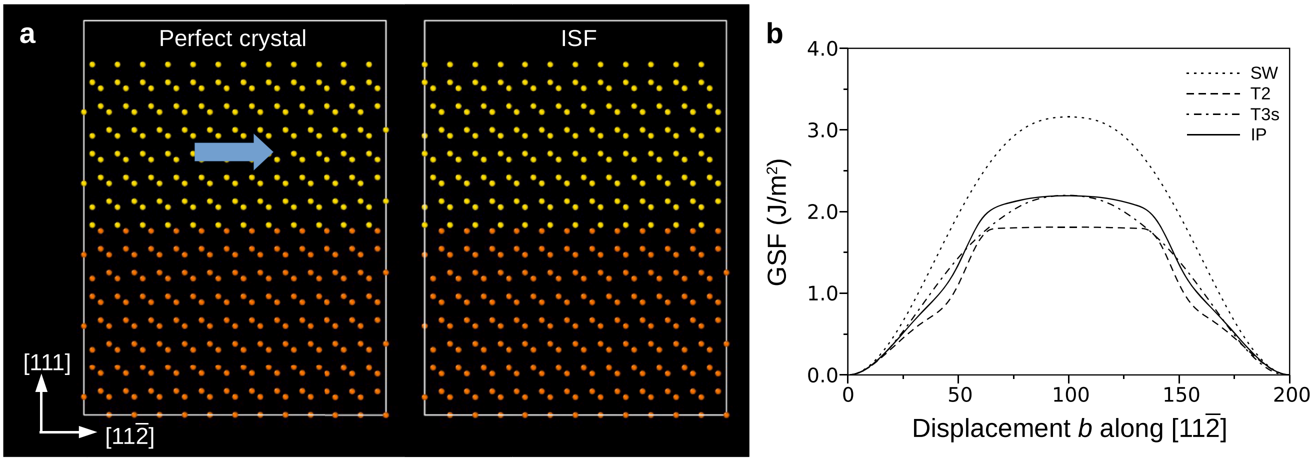

Fig. 2. Graphical demonstration of the applied GSFE method (a) and the simulation results (b). The upper part of the modelled Si-I supercell crystal was shifted in the direction indicated by the blue arrow (a) and transformed into Si-crystal with the ISF stacking fault. The results of GSFE simulations obtained with the Stillinger-Weber (SW), Tersoff (T2), screened Tersoff (T3s) and integrated (IP) atomic potentials appear in the form of energy-displacement curves (b). The SW and T2 curves constitute the upper and lower limit (b) for the IP-curve, since the latter inherits the properties of its components, *i.e.*, SW and T2 potentials.

particles selected for a structural analysis did not contain an equal number of atoms, we used normalized distribution N_i/N, where N stands for the number of atoms in a group under analysis. A similar procedure was used in the case of the RDF, with the interatomic distances investigated within the spherical volume of 5 Å radius.

3. Results

3.1. MD-simulations of indentation in Si with the Tersoff T2 potential

Our MD-simulations with the Tersoff T2 potential revealed an elastic-plastic transition in the original Si-I (cubic diamond, dc-1) structure at the contact pressure of p_c = 4.2 GPa and indentation depth of h = 13.5 Å (Figs. S1, S2a). The observed incipient plasticity is a phase transformation-governed phenomenon, similar to the one we have found in a nanodeformed GaAs crystal [50,51], and quite unlike the dislocation-governed incipient plasticity of the InP crystal [89]. Interestingly, the Si-I→Si-II' phase transition begins and continues directly under the loaded spherical indenter at a certain distance from the contact surface. Si-II' phase concerns the well-known Si-II structure, with slightly deviated structural parameters. Indeed, the atomic arrangement known as the Si-II was defined under standard, isotropic pressure, while the Si-II' revealed by our modelling is obviously distorted, having been formed under high non-isotropic stress during the nanoindentation process. The 'prime' sign is used throughout the paper to refer to any phase formed under high pressure during indentation.

The seed of the Si-II' phase shows up exactly in the area of enhanced shear strain (Figs. 3 and S2). As indentation proceeds, the nucleus continues to grow until the well-defined columns of the Si-II' phase formed, as illustrated in a 20 Å thin section across the region deformed under the contact pressure of p_c = 7.4 GPa and the contact depth of h = 39 Å (Fig. 3a). The Si-II' phase appears under the acting indenter in the form of vertical zones of different orientation, shown in Fig. 3a by successive numbers 1~6 (regions 1, 3 and 5 are rotated by approximately 10.5° in relation to sectors 2, 4 and 6). What we also find is that the tetragonal unit cell of the high-pressure Si-II' phase (Fig. 3b) is a distorted ($c/a \approx 1$) version of the well-known Si-II (β-Sn, $c/a = 0.55$) structure [90–92].

The structural difference between the Si-II' and Si-I phases is made explicit by the bond angle (BADF) and radial (RDF) distribution functions (Fig. 3c). The BADF analysis applied to Si-II' in different vertical zones as well as to the initial Si-I phase reveals the distinct Si-I peak at 109°, which promptly splits into two (100° and 145°) as indentation progresses. Furthermore, the RDF function confirms that the structure transformation did indeed take place. The sequence of characteristic peaks disclosed at the interatomic distance of 2.35, 3.84, and 4.50 Å, involves the Si-I structure, while the spectrum 2.35, 3.18, 3.58, 4.23, and 4.50 Å defines the Si-II' phase.

In summary, MD-simulations with the T2 potential succeed in modelling the transformation of Si-I to Si-II' phase, which corresponds to the experimentally determined [92] Si-II. However, the T2 fails to capture any dislocation activity in silicon across the whole range of depth that we have considered.

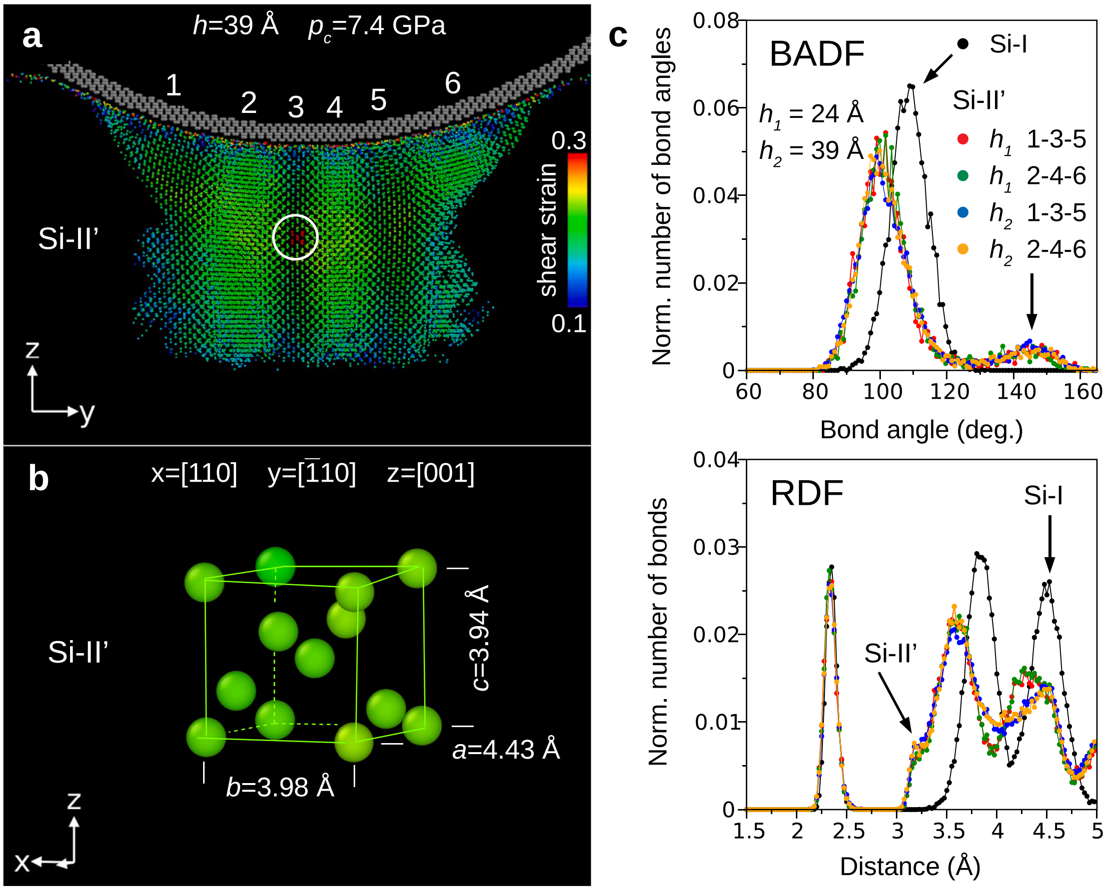

Fig. 3. Indentation-induced structure evolution of Si crystal modelled with the T2 potential. (a) The Si-II' structure detected in a 20 Å thin section along the axis z of indenter symmetry, across the transformed zone. Columns of the Si-II' structure, labelled 1-6, differ in orientation around their vertical axes by approx. 10.5°, while the colour of the Si atoms signals the atomic shear strain level. (b) The tetragonal unit cell detected in the circled area (a) points to the Si-II' structure. (c) BADF and RDF functions disclose characteristics of Si-I and phase, determined at h_1 = 24 Å and h_2 = 39 Å indentation depths, respectively.

3.2. MD-simulations of Si nanoindentation with the T3s potential

The structure evolution of a Si crystal under a spherical diamond tip begins with slight changes in Si-I structure at the indentation depth of $h = 14.5$ Å and contact pressure $p_c = 12.6$ GPa (Fig. S1). This initial transformation takes place at a distance of approx. 25 Å from the contact area, pointing to the dominant role of shear stress in the formation process. However, once the indentation depth reaches $h = 20$ Å, under the contact pressure of 15.9 GPa, the volume of a new high-pressure phase (dc-2, non-diamond) is sufficient to allow us its reliable identification (Fig. 4a and 4b), which turns out to be a distorted version of the BCT-5 structure [90,93].

As a matter of fact, the lattice of the dc-2 phase structure is by no means unique, as it might also be described as a highly compressed tetragonal unit cell of the initial Si-I phase (Fig. 4b). The dc-2 tetragonal lattice has the c/a ratio approaching unity, in contrast to the ideal, strain-free crystal for which $c/a = \sqrt{2}$. A good illustration of our findings is provided by the BADF and RDF functions whose peak sequences, characteristic of the dc-2 phase, equal 102°, 123° and 3.81, 4.0, 4.68 Å, respectively (Fig. 4c). The results are in contrast to those obtained using the T2 potential (Fig. 3c).

Further consideration of our MD-simulated nanoindentation has brought us to the conclusion that the sequence of the phase transformations is significantly affected by an increase of shear strain (Figs. 5a and S3).

The partial disappearance of the largely unstable dc-2 phase ($p_c = 17.8$ GPa, Fig. 5a) results in the formation of shear bands along the {111} planes followed by the development of Si-II and BCT-5 phases (Fig. 5a), whose characteristics broadly agree with earlier experiments and calculations [90–93]. The main difference between the unit cells of

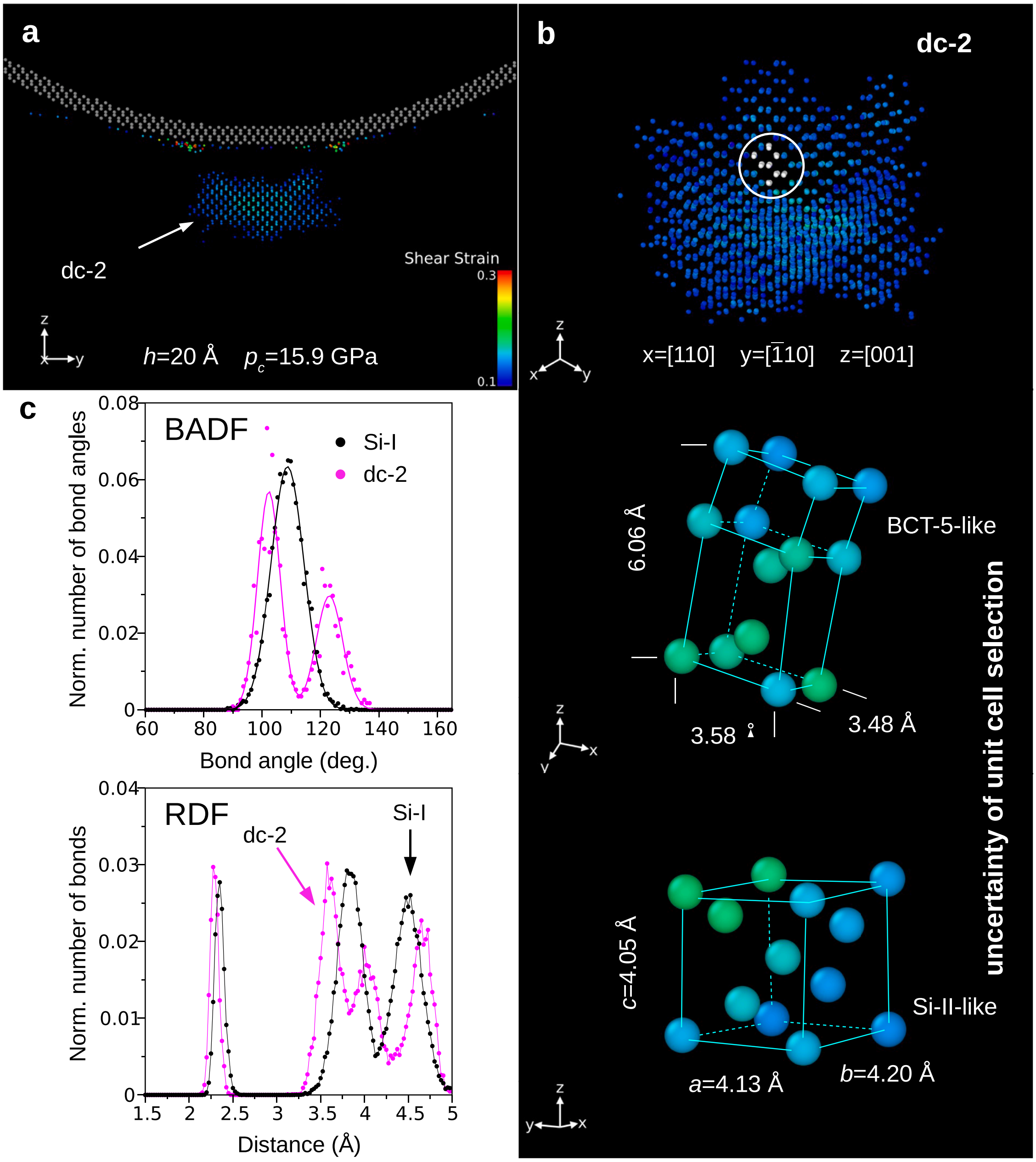

Fig. 4. Modelling with the T3s potential (atom colour specifies shear strain level). (a) High-pressure dc-2 phase positioned approx. 30 Å below the contact area. (b) Si structure rotated in such a way as to demonstrate the atom arrangement of the dc-2 phase area (marked here by a circle), which shows deviation from the BCT-5 structure [73]. An alternative view of the structure points towards a highly compressed tetragonal Si-I (dc-1) phase. (c) BADF and RDF functions at the $h = 20$ Å indentation depth, reveal differences between dc-2 and Si-I phases.

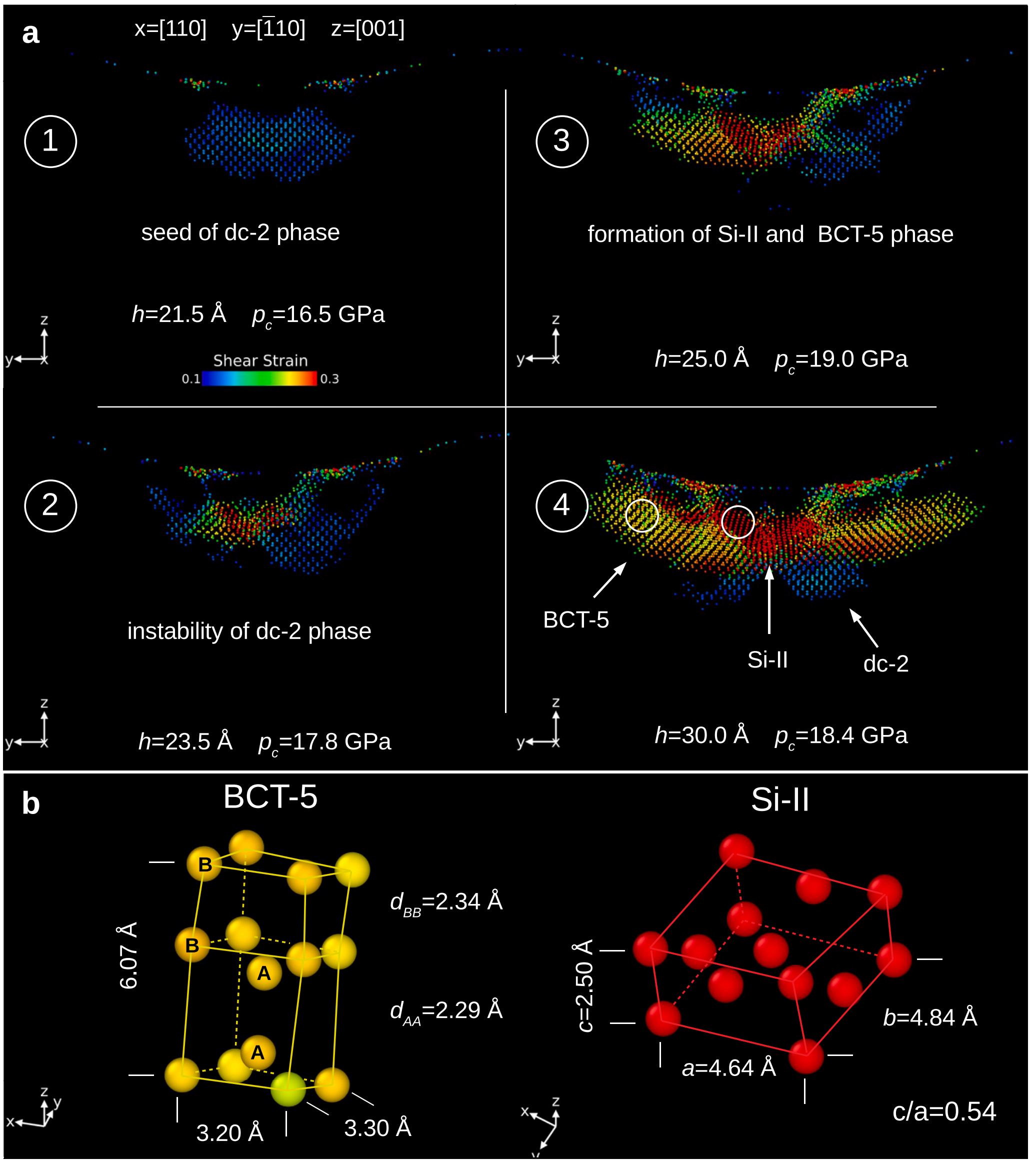

Fig. 5. Indentation-induced phase transformations in Si crystal modelled with the T3s potential. The selected indentation stages (snapshots 1∼4), show shear strain development and the resulting evolution of the high-pressure dc-2, Si-II and BCT-5 phases (a). A particular atom colour signals either shear strain level or the Si-II (red) and BCT-5 (yellow) phases. The {111} shear bands are formed in the late stages of indentation (snapshot 4). BCT-5 and Si-II phases (snapshot 4) are shown in focus as unit cells (b).

the dc-2 (Fig. 4b) and BCT-5 (Fig. 5b) consists in the former possessing a larger base than the latter, with a characteristic distortion in its upper part. Contrary to common belief, the Si-II phase shows up within the shear bands oriented along the {111} planes (Figs. 5a and S3) rather than in the material adjacent to the contact area [22,44].

Our visualization of the evolution of a strained atomic Si structure accomplished with the DXA-dislocation extraction algorithm [86] has enabled us to examine closely dislocation activity, which always accompanies nanoindentation in Si and has been reported widely on the basis of TEM (Transition Electron Microscopy) cross-section observations [17,20,22,43–46]. It is an advantage of the T3s potential to be able capture dislocation processes in tandem with phase transformations [70–72]. However, the DXA analysis has revealed but a few dislocations on the {111} planes (the Burger's vector 1/2<110>) which develop parallel to the (001) surface (Fig. 6). Furthermore, we have found no "downward defects", *i.e.*, moving in the direction opposite to the surface, despite numerous TEM reports of their existence [22,44,48].

All in all, while the results of our MD-simulations with the T3s potential agree with those obtained with the EAs and T3 potential [71,90, 91], we have found that using the T3s approach in Si nanodeformation is not without its drawbacks. These concern primarily the contact pressure necessary to initiate the Si-I→Si-II transformation (∼18 GPa), which is much overestimated compared to the ∼11 GPa level measured in anvil cell experiments [94], or ∼9.9 GPa derived from nanoindentation tests [48]. In addition, the Raman spectroscopy investigations undermine the possibility of the BCT-5 phase nucleation taking place at all during Si nanoindentation. Indeed, recent research [41,42] points to the existence of a distorted diamond cubic structure (dc-2) instead of the BCT-5, in contrast to the results of simulations with the T3s potential (Fig. 5).

To conclude, a visualization of nanodeformed Si crystal shows that nanoindentation induced changes modelled with the T3s screened potential are initiated by the Si-I→dc-2 transformation that precedes the formation of the Si-II and BCT-5 phases. The predicted dislocation structure is largely underdeveloped compared to microscopic observations [48].

3.3. MD-simulations with the integrated SW-T2 potential (IP)

The irreversible deformation of Si crystals begins with the nucleation of a tiny dc-2 phase seed (at the depth $h = 18$ Å and pressure $p_c = 7.7$ GPa - Fig. 7a, snapshot 1), analogously to the forecast made with the T3s potential (Fig. 5a - snapshot 1). In the same way, simulations with the IP, support the prediction that the nucleation of the dc-2 phase occurs in the volume, where the shear strain is increased.

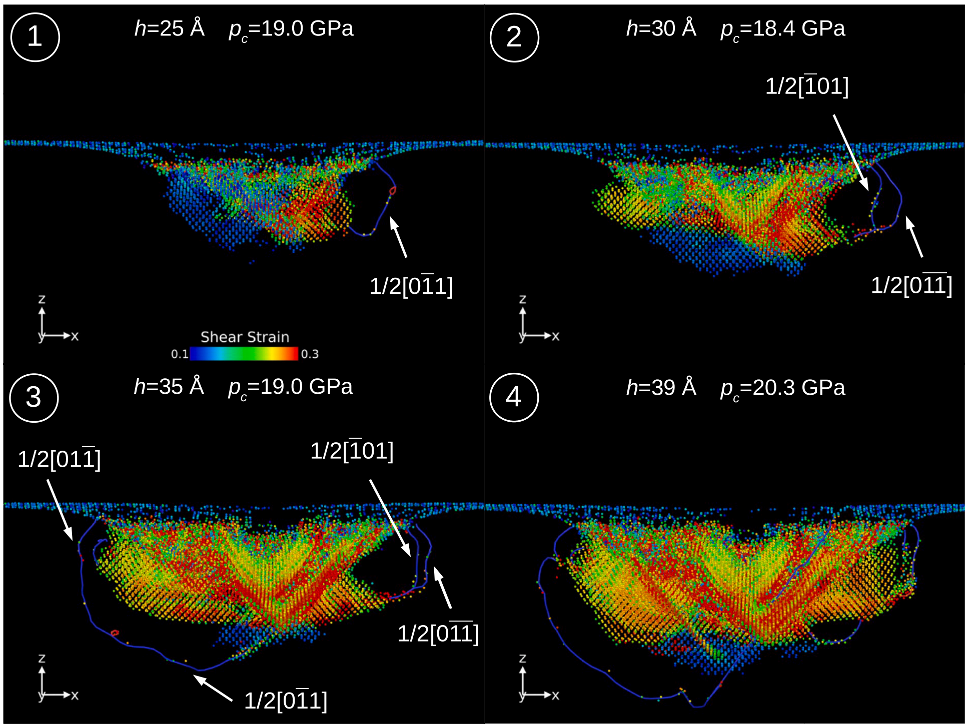

Fig. 6. Evolution of dislocation structure in nanoindentation deformed Si crystal modelled with the T3s potential. The sequence of structure-snapshots (from 1 to 4) taken for respective indentation depths of $h = 25$, 30, 35 and 39 Å provide the DXA based visualization of dislocation structure and its development. The linear defects (the Burger`s vector displayed in the figure) are generated in the {111} planes, parallel to the crystal surface and outside of the regions occupied by high-pressure Si phases.

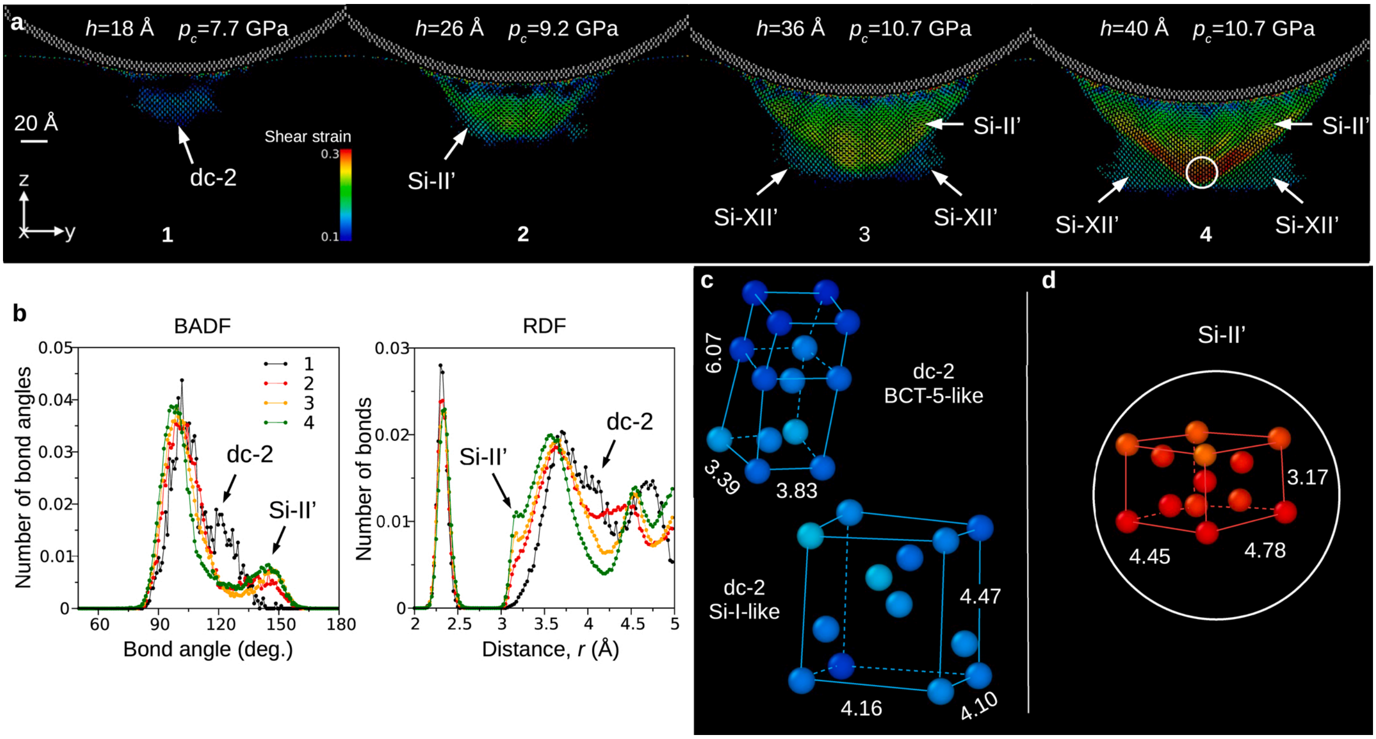

Fig. 7. Indentation-induced phase transformations of Si crystal modelled with the IP potential. (a) Structure evolution during consecutive indentation stages: $h = 18$, 26, 36 and 40 Å. The atoms of the original Si-I phase are not displayed. The 20 Å thin sections of the transformed zone show the dc-2 phase (snapshot 1), the Si-II' phase (snapshots 2 and 3), and illustrate the formation of the Si-XII' phase (snapshots 3 and 4), either directly under or in the vicinity of the Si-II' volume. (b) BADF and RDF functions for conditions in snapshots 1-4 excluding the Si-XII' structure. (c) The atomic arrangement in the detected dc-2 phase. The BCT-5-like and Si-I-like unit cells demonstrate alternative views of the dc-2 structure. (d) The c/a parameter determined for the Si-II' unit cell in the marked area [a white circle in panel (a)] achieves its lowest value of approx. 0.7.

As the indentation process unfolds, the detected high-stress structure grows, reaching a stage ($h = 26$ Å, $pc = 9.2$ GPa) when it undergoes the dc-2→Si-II' transition (Fig. 7a - snapshot 2). The resulting Si-II' expands further, forming a specific, compact seed of considerable volume adjacent to the contact area, in direct confirmation of the TEM observations by Wong *et al.* [22,43,44]. This very form of the new phase, with its cohesion and particular location, points towards effectiveness of the IP potential (compare: Figs. 5a and 7a, S3 and S4). Furthermore, as straining increases, part of the material with the Si-I structure, transforms into another crystalline structure, namely Si-XII’ (Fig. 7a, snapshots 3-4). This process takes place directly beneath, and outside, of the formed Si-II’.

The BADF and RDF analysis (Fig. 7b) of the atom arrangements, displayed in the consecutive snapshots (Fig. 7a), corroborates the sequence of crystal structure transformations that we have presented. Moreover, there is a perceivable resemblance between the BADF and RDF atomic distributions (excluding the Si-XII’ phase) derived with our IP potential for the Si-II’ structure (Fig. 7b) and those obtained by means of the T2 potential (Fig. 3c). The same applies to the dc-2 phase, which the IP computer experiments have revealed in a similar way as has the T3s potential (compare Figs. 7b and 4c). This allows us to conclude that the integrated IP approach - by combining the strengths of both the T2 or SW potentials – provides a valuable and precise means of predicting silicon structure during nanoscale deformation.

In order to gain a detailed picture of the results obtained with the IP potential, we have scrutinized the atomic arrangements of the dc-2 and Si-II’ phases (Fig. 7c and 7d), which reflect alternative ways of describing the dc-2 phase. We found the tetragonal parameter of the Si-II’ phase achieving its lowest value at $c/a \approx 0.7$. Moreover, the Si-II’ structure displays a higher value of c/a ratio in the proximity of the contact surface (approx. ~0.88 refer to Fig. S4). The formation of Si-XII’ phase predicted by our MD-simulations with the integrated IP potential (refer to Fig. 7a - snapshot 3 and 4) requires a separate elaboration. The nucleation of this specific structure occurs at a late stage of nanoindentation in four distinct zones which our visualisation of the deformed atomistic arrangement reveals (Fig. 8a).

In order to obtain a clear image of the detected Si-XII’ structure, we have examined three mutually orthogonal projections of the lattice (Fig. 8a), whose uniqueness is confirmed by the BADF and RDF functions (Fig. 8b). The characteristic BADF peaks of the Si-XII’ phase is located at 94°, 109° and 132°, while those of RDF are positioned at 3.4, 3.9, 4.3 and 4.9 Å. Both RDF and BADF data are thus consistent with the theoretical spectra for the Si-XII phase (Fig. 8b and Table S1). In particular, the peak in the BADF-spectrum for a bond angle of 132° (Fig. 8b), which we regard as a characteristic of the Si-XII’, corresponds to the one at 137° standard for a perfect Si-XII structure [95].

We investigated in greater detail the local atomic arrangement of both the Si-XII’ (Fig. 8c) and Si-XII (Fig. 8d) structures. The atoms highlighted by white circles (Fig. 8c, d) show up closer to the surface, whereas the remaining ones are deeper in; those labelled 1 and 2 are placed in the centre of the volume of the unit cell. The interatomic distance and bond angles calculated for both the Si-XII’ and Si-XII structures are listed in Fig. 8. The main difference between the discussed arrangements resides in the positioning of the atoms labelled 1, 6, 7, 8 (Fig. 8). A perceptible symmetry among the bond angles of the Si-XII’ phase is not displayed in the Si-XII phase. It may be presented as follows: $\theta_{2'1'6'} \approx \theta_{1'2'4'}$, $\theta_{2'1'7'} \approx \theta_{1'2'3'}$, and $\theta_{2'1'8'} \approx \theta_{1'2'5'}$. The highest bond angle of about 137° appears twice ($\theta_{1'2'3'}$, $\theta_{2'1'7'}$) within the Si-XII’ unit cell, in contrast to the atomic arrangement of the Si-XII phase, where the same angle appears only for the atoms 1,2 and 3. It is possible to arrive at the Si-XII atomic arrangement, using a single bond angle of 137°, provided the atoms labelled 6′,7′, 8′ are rotated around the axis

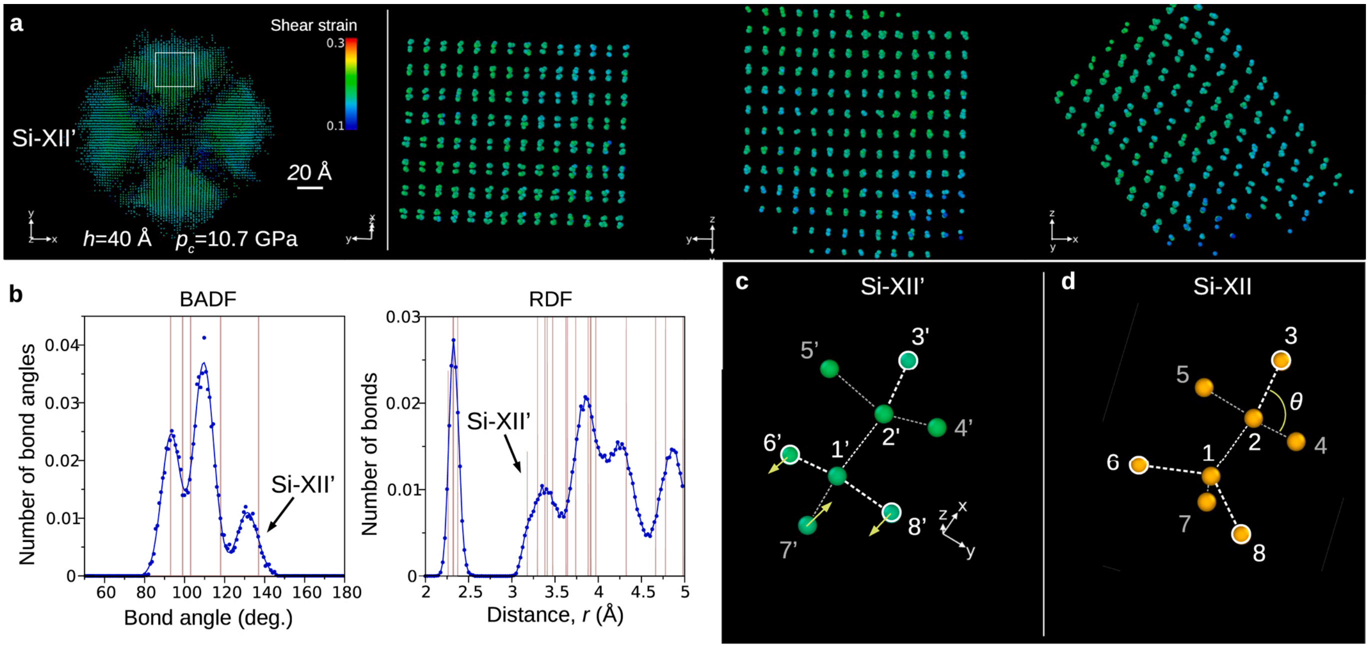

Si-XII’	2’	3’	4’	5’	6’	7’	8’
1’	2.438				2.305	2.280	2.220
2’		2.392	2.380	2.310			
1’2’		136	109	94			
2’1’					103	138	89

Si-XII	2	3	4	5	6	7	8
1	2.318				2.318	2.262	2.318
2		2.325	2.325	2.373			
12		137	103	93			
21					118	99	118

Fig. 8. Modelling with the integrated IP potential: The details of Si-XII’ structure (a) The volume of the Si-XII’ phase consists of four separate parts. (b) Three orthogonal views of the Si-XII’ structure selected from the region marked with a white circle. (c) The results of the BADF and RDF analysis show the differences between the three high-pressure Si phases modelled by integrated potential. The BADF and RDF of Si-XII’ phase exhibit peaks cantered at distances near those expected for real Si-XII phase (brown lines, Table S1). The data displayed beneath the figures (a) and (b) expose differences in the atomic arrangement of the Si-XII’ and Si-XII phases.

passing through the atom 1′, located in the plane of the figure and perpendicular to the segment 1′2′. The yellow arrows in Fig. 8c mark positions of the atoms after such a rotation, thus exposing the Si-XII’ structure as a characteristically deformed Si-XII phase. A scenario of this kind is likely to occur in highly inhomogeneous stress induced under the acting indenter.

An obvious advantage of the IP potential in MD-simulations lies in the prospect of modelling both phase transformations and dislocation processes simultaneously. Fig. 9 presents nucleation and a well-developed dislocation structure captured at the indentation depth of $h = 43$ Å ($p_c = 11.4$ GPa) and $h = 45$ Å ($p_c = 11.5$ GPa) together with high-pressure phases that exist at this stage of nanodeformation of an Si crystal. DXA analysis of the atomistic arrangement enables us to identify the dislocation lines in the {111} planes, and to define their Burger’s vectors as 1/2<110>. It is also worth noting that dislocations assume the correct orientation, namely, downwards into the crystal volume, which agrees with experimental observations [42,48,96]. Significantly, MD-simulations using our Integrated Potential did not produce dislocations parallel to the indented surface, in contrast to outcomes using the T3s potential; MD-simulations using the T2 potential, on the other hand, failed entirely to mirror lattice defects activity.

We also included the unloading process in our MD-simulations – something rarely undertaken in MD-modelling of the nanoindentation of silicon crystal. Starting with the Si structure under a maximum load (*e. g.*, snapshot 4 in Fig. 7a), we simulated shift of the indenter tip vertically up, with a depth increment of $\Delta h = 0.5$ Å, leading to a gradual disappearance of the high-pressure silicon crystalline phases. After complete unloading, the only dislocation net and volume of the amorphous Si phase remained in the vicinity of a residual indent (Fig. 10). The depth of the simulated residual impression equalled approximately $h_r = 7$ Å, while the amorphous Si occupied an approximate V-shaped cross-section between 23 Å and 97 Å from the crystal surface.

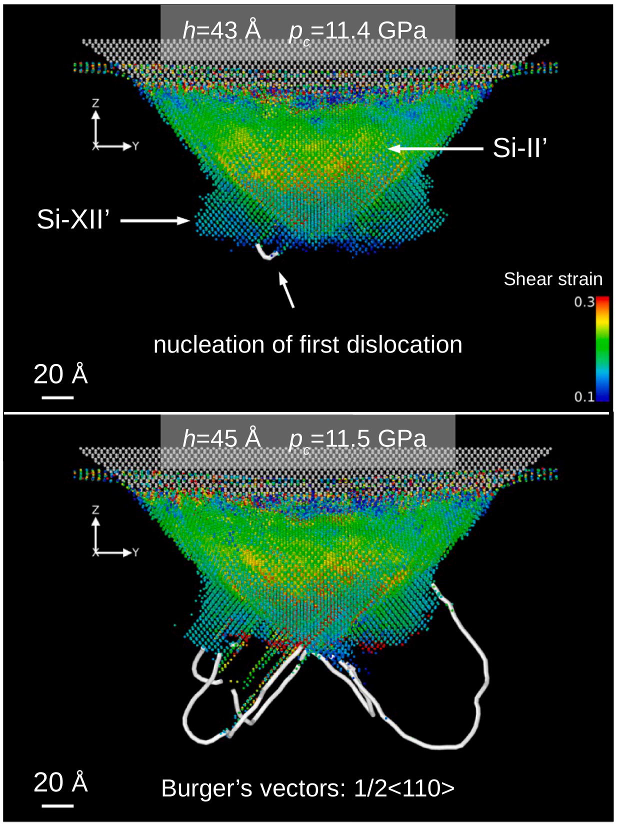

Fig. 9. Modelling with the integrated IP potential: visualization of a pattern of displacements, revealing nucleation and the development of dislocations. The dislocation lines are situated in the {111} planes with the Burger’s vectors 1/2<110>.

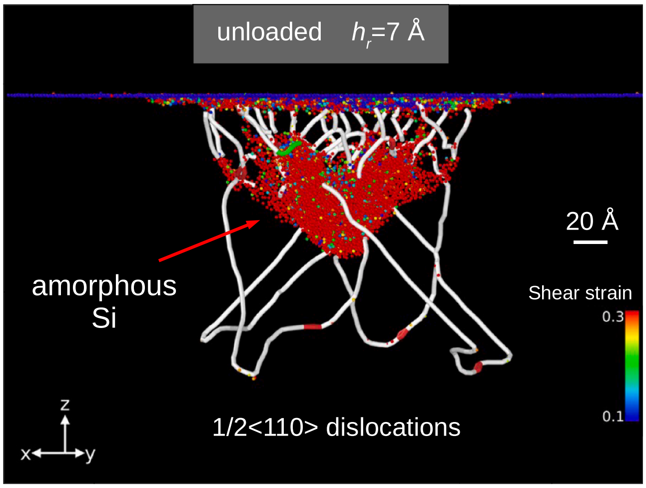

Fig. 10. MD-simulations with IP potential: The residual structure of the deformed Si crystal obtained after complete unloading. The detected features consist of a dislocation network (white lines) and amorphous phase volume (red atoms) located at distance of 23 Å from the residual impression. The dislocations with Burger’s vector mainly 1/2<110> (white curves) begin and terminate either in an amorphous phase, or crystal surface.

4. Discussion

Our evidence consists of two complimentary parts: the first puts forward a method of constructing the integrated SW-T2 interatomic potential (IP); the second demonstrates that MD simulations of Si nanodeformation with the IP potential are able to mimic the response of Si more faithfully than other potentials in common use. In general, despite its simplicity the introduced procedure of selecting a universal and robust potential meets all the criteria stipulated by Harrison *et al.* [32] such as simplicity, accuracy, enhanced transferability and computational speed. Significantly, our integrated potential IP inherits the characteristics of its constituent parts: the elastic constants we obtained for the Si-I structure (Table 1) follow the weighted sum of the ones derived by means of the SW and T2 potentials. By comparing our outcome with that of the T3s - presently the most advanced model for studying the mechanical behaviour of nanoscale strained Si crystal [65, 71] – we demonstrate that the IP result represents a better match with the experimental reality.

That the integrated SW-T2 potential preserves the characteristics of its constituent parts, becomes evident in MD simulations of the structural changes which occur in Si during spherical nanoindentation. The results of our calculations indicate that modelling with the IP allows the capture of the subtle interplay between phase transformation and the generation of linear defects, which the T2 and SW potentials can also model, each in its own right. However, the SW potential, while performing well at modelling dislocation activity, fails to reflect the high-pressure crystalline phases of Si. Similarly, the T2 potential, which is only used to model the Si-I→Si-II’ phase transformation (Fig. 3).

Whether plastic deformation of Si is initiated by defect generation or phase transformation has been a matter of controversy for decades [17, 20,22,40–48,64,70–72,97,98]. For instance, Wong *et al.* [22,44] maintain that the irreversible deformation of an Si crystal is induced by spherical indentation (tip diameter of ~21.5 μm) is of “a stochastic kind”, and thus seems to be caused either by phase transition or the generation of dislocations. All the same, their work is worthy of attention, since it approaches the issue of incipient plasticity in nanoindented Si, in a methodical and persuasive manner. Accordingly, Wong et al. witnessed Si plasticity being steered by the transformation in a compact mass adjacent to the acting tip [22,44], which is also borne out by our simulations with the IP potential (Figs. 7a and 9).

To be more precise, our MD-prediction envisages the formation of a single, relatively large volume of what we term the Si-II' phase (Fig. 7a and 7d) directly under the acting spherical indenter. This is in contrast to the results obtained using T3s potential, which generates isolated areas of the Si-II structure (Figs. 5a and S3) distributed within shear bands. The generation of the Si-II' structure modelled by means of the integrated IP potential (Fig. 7a) is volumetric in character as opposed to local, such as the formation of the Si-II dispersed within V-shaped shear bands (Fig. S3). It is therefore reasonable to assume that the Si-I→Si-II transformation modelled by the T3s potential is governed predominantly by sheer stress, whereas that from the Si-I into Si-II' (IP model) by hydrostatic one.

In situ observations of the structural changes in a nanoindentation-deformed Si crystal have been performed by means of the Raman spectroscopy [40–42] and combined with a microscopic inspection and structural analysis of the material close to the residual indents [17,20,22,43–46]. Thus, Gerbig *et al.* [41] have been able to provide experimental proof that the Si-I→Si-II transition detected during the loading cycle does not proceed in a direct but gradual manner, since it is accompanied by the formation of the dc-2 structure, which has been referred to as a “severely distorted Si-I phase”. The dc-2 had earlier been mistaken [40] for the BCT-5 based on MD-simulations with the non-screened Tersoff type potential [88,89].

The results of our calculations with the IP and T3s potentials point to the formation of the Si-II' and Si-II, respectively. In each case, this is preceded by the initial transition from the Si-I to a high-pressure dc-2 phase. The ambiguity contained in the description of the simulated dc-2 phase (Figs. 3b and 7c) parallels that of the Raman spectra found by Gerbig *et al.* [40,41]. It is worth emphasising, however, that the BCT-5 phase does not show up for late stages of indentation in simulations performed with IP potential (Fig. 7) as opposed to the T3s (Fig. 5). The result is supported by a recent Raman spectroscopy examination of nanoindentation-deformed Si crystals [41,42].

Our main point of reference with regard to the IP is the screened T3s potential, which to this day represents the most advanced approach to the complex nanodeformation of Si crystals, accounting both for dislocation activity as well as stress-induced phase transformations [70–72]. Thus, both the T3s- (Fig. 6) and IP- (Fig. 9) driven MD-simulations reveal dislocation activity that contributes to the overall indentation deformation, in addition to phase transformations. However, there are some crucial differences between the two. In the scenario obtained with the integrated potential, slip leads to the generation of large, extended linear defects on the {111} planes that develop outwardly of the Si volume occupied by high pressure Si-II'/Si-XII' phases (Fig. 9). The situation looks different in the case of the T3s potential where slip, while also occurring along the {111} planes, generates limited dislocations in the direction parallel to the (001) surface of the deformed Si crystal (compare Figs. 6 and 9). This remarkable difference is related to the energy consumption in a nanoindentation deformed Si crystal during its irreversible deformation. The total elastic energy E_{el} stored in a deformed crystal consists of a volumetric part $E_{el,h}$ - associated with the hydrostatic stress, and $E_{el,s}$ - related to the acting shear stress. The volumetric character of the Si-I→Si-II' transformation deduced with the IP potential suggests that the process is mainly at the expense of $E_{el,h}$'s. Consequently, the remaining $E_{el,s}$ part is used up for the generation of dislocations. By contrast, the shear stress-steered Si-I→Si-II transformation, modelled with the T3s potential consumes the lion’s share of the $E_{el,s}$ energy, resulting in its deficiency for the generation of a sizable dislocation network (compare our Fig. 6 and the experimental data displayed either as Figs. 2 and 3 in [48] or Fig. 4 in [96]).

Another point worth noting is that the attributes of the integrated IP potential enabled the detection of the high-pressure Si-XII structure already in the late stages of the loading cycle (Figs. 7 and 8). The presence of this phase was not revealed by the previous reports on MD simulation of nanoscale indentation in silicon [68–73]. Remarkably, modelling with the IP potential reflects the Si-XII (r8) arrangement detected experimentally in the course of unloading, however [40,94]. We have been able to come across only one publication to locate the Si-XII structure in the loading stage, namely by Gerbig *et al.* [42], where it appears in the Raman spectrum taken at the load $P = 50$ mN (see Figs. 2 and 3 in [42]).

The structure of the deformed section of the Si crystal, shown in Fig. 10, merits particular attention. It will be seen that modelling with the IP potential manages to capture both the amorphous phase as well as a fully-fledged dislocation-structure of silicon, thus confirming numerous experimental observations by means of TEM [48]. This demonstrates the IP`s exceptional ability to portray the structural changes that occur in silicon under inhomogeneous stress induced by nanoindentation.

Successful detection of the development of Si-XII phase during nanoindentation loading of Si crystal constitutes one of the crucial advantages of the IP potential. The accomplishments in reflecting experimentally observed - high-pressure Si phases, dislocations and phase transformation sequences, encourages future application of the IP-based simulations to uncovering the unknown processes activated in nanoscale deformed semiconductors.

5. Conclusions

In summary, we have managed to propose a reliable integrated interatomic IP potential of remarkable readiness, enabling modelling of the entire complex of phenomena that occur in nanoindentation-deformed Si crystals in conformity with the results of earlier experiments. MD simulations with IP provide a realistic contact stress at the onset of a plastic deformation of silicon and correctly predict the essential role of a high-pressure dc-2 phase formation in all its crystallographic complexity (as a highly-compressed Si-I structure or a distorted BCT-5 phase). Moreover, an integrated potential makes it possible - again in accordance with earlier experiments - to reflect the subsequent stages of Si nanodeformation, *i.e.*, a further transformation to the Si-II' phase ($c/a \approx 0.66$), the formation of an Si-XII' structure as deformation proceeds and, finally, the activation of dislocation processes. The predicted formation of Si-XII demonstrates important advantage of our IP method as compared to previous MD-simulations utilizing other potentials. The demonstrated ability to predict the observed phase transformation sequences in Si and accompanied dislocation processes inspire future relevance of our IP method to uncovering unknown developments in nanoscale stressed semiconductors. Importantly, the IP method may increase the transferability of the existing potentials. In terms of efficiency, the method is both fast and sparing of computational resources, even in a comparison with machine-learning potentials. Furthermore, the IP method has been shown to apply to different physical phenomena, suggesting it might be an alternative for some of the available potentials. The IP method’s ready availability will satisfy the demand for a quick way to construct interatomic potentials and open up the vast library of the existing ones to new applications. Last but not least, we hope our results regarding silicon, in particular the precision and accuracy in forecasting stress-induced atomistic structure evolution, will prove relevant to nanomechanical studies of semiconductors more generally, and that the IP approach will deserve its place in the contemporary research toolbox of materials modelling.

Data availability

All relevant data supporting the key findings of this study are available within the article and its Supplementary Information files or from the corresponding author upon reasonable request.

Supplementary material

Supplementary material associated with this article can be found, in the online version, at … doi???

Declaration of Competing Interest

The authors declare that they have no known competing financial interests or personal relationships that could have appeared to influence the work reported in this paper.

Acknowledgments

RA thanks Dr Li-Fang Zhu (Max-Planck-Institut für Eisenforschung GmbH) and Dr Jan Janssen (Los Alamos National Lab) for access to their programs essential to the calculations. RN is grateful to Prof. Toshihiro Shimada (Hokkaido University) and Prof. Adam Poludniak (Seirei University) for important discussions. He also expresses appreciation to Prof. Koichi Niihara (Nagaoka University of Technology), Prof. Tohru Sekino (Osaka University) as well as Prof. Naoya Nishimura (Meijo University) for their long-standing support with computational modelling of ceramics and semiconductors. We thank also Mr. Michael Berg (Bruker Nano Surfaces, Los Angeles) for his valuable remarks on nanoindentation experiments. We wish to express our deep appreciation to Mr Thomas Wyrobek, the President of Hysitron. Inc., and his team for being of invaluable assistance and inspiration to our Nordic Hysitron Laboratory at Alto University over the past two decades.

This research was assisted by the Academy of Finland - Research Platform OMA for Programmable Materials (The Consortium PROPER). DC is grateful for the support from the National Science Centre, Poland (Grant No. 2016/21/B/ST8/02737). All computer simulations used resources provided to the Nordic Hysitron Laboratory by the CSC-IT Centre for Science, Finland, which we gratefully acknowledge. RN appreciates the visiting scholar opportunity at Hokkaido University and Meijo University.

Supplementary materials

Supplementary material associated with this article can be found, in the online version, at doi:10.1016/j.mtla.2023.101761.

References

[1] W. O'Mara, R.B. Herring, L.P. Hunt, Handbook of Semiconductor Silicon Technology (2007).
[2] H.G. Craighead, Nanoelectromechanical systems, Science 290 (2000) 1532–1535.
[3] A.A. Giardini, A study of the directional hardness in silicon, The Am. Mineral. 43 (1958) 957–969.
[4] A.P. Gerk, D. Tabor, Indentation hardness and semiconductor-metal transition of germanium and silicon, Nature 271 (1978) 732–733.
[5] K.E. Petersen, Silicon as a mechanical material, Proc. IEEE 70 (1982) 420–457.
[6] J.J. Gilman, Flow of covalent solids at low temperatures, J. Appl. Phys. 46 (1975) 5110–5113.
[7] J.J. Gilman, Why silicon is hard? Science 261 (1993) 1436–1439.
[8] D.R. Clarke, M.C. Kroll, P.D. Kirchner, R.F. Cook, B.J. Hockey, Amorphization and conductivity of silicon and germanium induced by indentation, Phys. Rev. Lett. 60 (1988) 2156–2159.
[9] R.W. Armstrong, W.H. Robinson, Combined elastic and plastic deformation behaviour from a continuous indentation hardness test, New Zealand J. Sci. 17 (1974) 429–437.
[10] D. Newey, M.A. Wilkins, H.M. Pollock, An ultra-low-load penetration hardness tester, J. Phys. E: Sci. Instrum. 15 (1982) 119–122.
[11] J.B. Pethica, R. Hutchings, W.C. Oliver, Hardness measurement at penetration depths as small as 20 nm, Philos. Mag. A 48 (1983) 593–606.
[12] G.M. Pharr, W.C. Oliver, D.R. Clarke, Hysteresis and discontinuity in the indentation load-displacement behavior of silicon, Scr. Mater. 23 (1989) 1949–1952.
[13] T.F. Page, W.C. Oliver, C.J. Mchargue, The deformation-behavior of ceramic crystals subjected to very low load (nano) indentations, J. Mater. Res. 7 (1992) 450–475.
[14] E.R. Weppelmann, J.S. Field, M.V. Swain, Observation, analysis, and simulation of the hysteresis of silicon using ultra-micro-indentation with spherical indenters, J. Mater. Res. 8 (1993) 830–840.
[15] D.L. Callahan, J.C. Morris, The extent of phase transformation in silicon hardness indentations, J. Mater. Res. 7 (1992) 1614–1617.
[16] L.J. Vandeperre, F. Giuliani, S.J. Lloyd, W.J. Clegg, Mechanisms controlling the hardness of Si and Ge, MRS Proc. 795 (2004). U8–221–U822–6.
[17] V. Domnich, Y. Gogotsi, S. Dub, Effect of phase transformations on the shape of the unloading curve in the nanoindentation of silicon, Appl. Phys. Lett. 76 (2000) 2214–2216.
[18] T. Juliano, V. Domnich, Y. Gogotsi, Examining pressure-induced phase transformations in silicon by spherical indentation and Raman spectroscopy: a statistical study, J. Mater. Res. 19 (2004) 3099–3108.
[19] J. Jang, M.J. Lance, S. Wen, T.Y. Tsui, G.M. Pharr, Indentation-induced phase transformations in silicon: influences of load, rate and indenter angle on the transformation behavior, Acta Mater. 53 (2005) 1759–1770.
[20] S. Ruffell, J.E. Bradby, J.S. Williams, P. Munroe, Formation and growth of nanoindentation-induced high pressure phases in crystalline and amorphous silicon, J. Appl. Phys. 102 (2007), 063521.
[21] M.S.R.N. Kiran, B. Haberl, J.S. Williams, J.E. Bradby, Temperature-dependent deformation mechanisms in pure amorphous silicon, J. Appl. Phys. 115 (2014), 113511.
[22] S. Wong, B. Haberl, J.S. Williams, J.E. Bradby, Phase transformation as the single-mode mechanical deformation of silicon, Appl. Phys. Lett. 106 (2015), 252103.
[23] M.S.R.N. Kiran, T.T. Tran, L.A. Smillie, B. Haberl, D. Subianto, J.S. Williams, J. E. Bradby, Temperature-dependent mechanical deformation of silicon at the nanoscale: Phase transformation versus defect propagation, J. Appl. Phys. 117 (2015), 205901.
[24] Y. Hong, N. Zhang, M.A. Zaeem, Metastable phase transformation and deformation twinning induced hardening-stiffening mechanism in compression of silicon nanoparticles, Acta Mater. 145 (2018) 8–18.
[25] H. Babei, V. Levitas, Effect of 60o dislocation stresses, nucleation and growth for phase transformations between silicon I and silicon II under triaxial loading: phase field study, Acta Mater. 177 (2019) 178–186.
[26] H. Nobarani, N. Zhang, M.A. Zaeem, Nanotwin-induced strengthening in silicon: a molecular dynamics study, Acta Mater. 189 (2021), 105990.
[27] J.C.H. Spence, Atomistic and mechanical properties of silicon, Acta Mater. 161 (1999) 4153–4159.
[28] J. Guenole, S. Brochard, J. Godet, Unexpected slip mechanism induced by the reduced dimensions in silicon nanostructures: atomistic study, Acta Mater. 59 (2011) 7464–7472.
[29] X. Du, H. Zhao, L. Zhang, Y. Yang, H. Xu, H. Fu, L. Li, Molecular dynamics investigations of mechanical behaviour in monocrystalline silicon due to nanoindentation at cryogenic temperatures and room temperature, Sci. Rep. 5 (2015) 16275.
[30] S. Goel, A. Kovalchenko, A. Stukowski, G. Cross, Influence of microstructure on the cutting behaviour of silicon, Acta Mater. 105 (2016) 464–478.
[31] A. Merabet, M. Texier, C. Tromas, S. Brochard, L. Pizzagali, L. Thilly, J. Rabier, A. Talneau, Y. Vaillant, O. Thomas, J. Godet, Low-temperature intrinsic plasticity in silicon at small scales, Acta Mater. 161 (2018) 54–60.
[32] J.A. Harrison, J.D. Schall, S. Maskey, P.T. Mikulski, M.T. Knippenberg, B. H. Morrow, Review of force fields and intermolecular potentials used in atomistic computational materials research, Appl. Phys. Rev. 5 (2018), 031104.
[33] S.Z. Chavoshi, X. Shuozhi, Nanoindentation/scratching at finite temperatures: Insights from atomistic-based modelling, Progress Mater. Sci. 100 (2019) 1–20.
[34] S.M. Rassoulinejad-Mousavi, Y. Zhang, Interatomic potentials transferability for molecular simu-lations: a comparative study for platinum, gold and silver, Sci. Rep. 8 (2018) 2424.
[35] J.G. Lee, Computational Materials Science: An Introduction, CRC-Press, Taylor & Francis, 2017.
[36] D. Munk, M. Katzman, M. Hen, M. Priel, M. Feldberg, T. Sharabani, S. Levy, A. Bergman, A. Zadok, Surface acoustic wave photonic devices in silicon on insulator, Nat. Comm. 10 (2019) 4214.
[37] C. Roques-Carmes, S. Kooi, Y. Yang, A. Massuda, P. Keathley, A. Zaidi, Y. Yang, J. Joannopoulos, K. Berggren, I. Kaminer, M. Soljačić, Towards integrated tunable all-silicon free-electron light sources, Nat. Comm. 10 (2019) 3176.
[38] R. Achal, M. Rashidi, J. Croshaw, D. Churchill, M. Taucer, M.C.T. Huff, J. Pitters, R. Wolkow, Lithography for robust and editable atomic-scale silicon devices and memories, Nat. Comm. 9 (2018) 2778.
[39] H. Nalwa (Ed.), Silicon-Based Materials and Devices (2001).
[40] Y. Gerbig, C. Michaels, A. Forster, R. Cook, In situ observation of the indentation-induced phase transformation of silicon thin films, Phys. Rev. B 85 (2012), 104102.
[41] Y. Gerbig, C. Michaels, R. Cook, In situ observation of the spatial distribution of crystalline phases during pressure-induced transformations of indented silicon thin films, J. Mater. Res. 30 (2015) 390–406.
[42] Y. Gerbig, C. Michaels, R. Cook, In situ observations of berkovich indentation induced phase transitions in crystalline silicon films, Scr. Mater. 120 (2016) 19–22.
[43] S. Wong, B. Haberl, J. Williams, J. Bradby, The influence of hold time on the onset of plastic deformation in silicon, J. Appl. Phys. 118 (2015), 245904.
[44] S. Wong, B. Haberl, J. Williams, J. Bradby, Phase transformation dependence on initial plastic deformation mode in Si via nanoindentation, Exp. Mechan. 57 (2017) 1037–1043.
[45] S. Wong, B. Johnson, B. Haberl, A. Mujica, J. McCallum, J. Williams, J. Bradby, Thermal evolution of the indentation-induced phases of silicon, J. Appl. Phys. 126 (2019) 1–10.
[46] S. Wong, B. Haberl, B. Johnson, A. Mujica, M. Guthrie, J. McCallum, J. Williams, J. Bradby, Thermal evolution of the indentation-induced phases of silicon, Phys. Rev. Lett. 122 (2019), 105701.

[47] R. Abram, D. Chrobak, R. Nowak, Origin of a nanoindentation pop-in event in silicon crystal, Phys. Rev. Lett. 118 (2017), 095502.

[48] J. Bradby, J. Williams, J. Wong-Leung, M. Swain, P. Munroe, Transmission electron microscopy observation of deformation microstructure under spherical indentation in silicon, Appl. Phys. Lett. 77 (2000) 3749–3751.

[49] D. Chrobak, J. Räisänen, R. Nowak, Effect of silicon on the elastic-plastic transition of GaAs crystal, Scr. Mater. 102 (2015) 31–34.

[50] R. Nowak, D. Chrobak, S. Nagao, D. Vodnick, M. Berg, A. Tukiainen, M. Pessa, An electric current spike linked to nanoscale plasticity, Nat. Nanotechnol. 4 (2009) 287–291.

[51] D. Chrobak, K. Nordlund, R. Nowak, Nondislocation origin of GaAs nanoindentation pop-in event, Phys. Rev. Lett. 98 (2007), 045502.

[52] M. Fujikane, T. Yokogawa, S. Nagao, R. Nowak, Nanoindentation study on insight of plasticity related to dislocation density and crystal orientation in GaN, Appl. Phys. Lett. 101 (2012), 201901.

[53] M. Fujikane, S. Nagao, D. Chrobak, T. Yokogawa, R. Nowak, Room-temperature plasticity of a nanosized GaN crystal, Nano Lett. 21 (2021) 6425–6431.

[54] J. Michelin, L. Gonçalves, J. Rino, On the transferability of interaction potentials for condensed phases of silicon, J. Molecular Liq. 285 (2019) 488–499.

[55] A. Bartók, J. Kermode, N. Bernstein, G. Csányi, Machine learning a general-purpose interatomic potential for silicon, Phys. Rev. X 8 (2018), 041048.

[56] Y. Mishin, Machine-learning interatomic potentials for materials science, Acta Mater. 214 (2021), 116980.

[57] F. Stillinger, T. Weber, Computer simulation of local order in condensed phases of silicon, Phys. Rev. B 31 (1985) 5262–5271.

[58] J. Tersoff, New empirical model for the structural properties of silicon, Phys. Rev. Lett. 56 (1986) 632.

[59] J. Tersoff, New empirical approach for the structure and energy of covalent systems, Phys. Rev. B 37 (1988) 6991–7000.

[60] J. Tersoff, Empirical interatomic potential for silicon with improved elastic properties, Phys. Rev. B 38 (1988) 9902–9905.

[61] J. Tersoff, Modeling solid-state chemistry: Interatomic potentials for multicomponent systems, Phys. Rev. B 39 (1989) 5566. ?

[62] M. Bazant, E. Kaxiras, J. Justo, Environment-dependent interatomic potential for bulk silicon, Phys. Rev. B 56 (1997) 8542–8552.

[63] K. Albe, P. Erhart, Analytical potential for atomistic simulations of silicon, carbon, and silicon carbide, Phys. Rev. B 71 (2005) 35211.

[64] Y. Kumagai, S. Izumi, S. Hara, S. Sakai, Analytical potential for atomistic simulations of silicon, carbon, and silicon carbide, Comp. Mater. Sci. 39 (2007) 457–464.

[65] L. Pastewka, A. Klemenz, P. Gumbsch, M. Moseler, Screened empirical bond-order potentials for Si-C, Phys. Rev. B 87 (2013), 205410.

[66] H. Balamane, T. Halicioglu, W. Tiller, Comparative study of silicon empirical interatomic potentials, Phys. Rev. B 46 (1992) 2250–2279.

[67] J. Godet, L. Pizzagalli, S. Brochard, P. Beauchamp, Comparison between classical potentials and ab initio methods for silicon under large shear, J. Phys. Condens. Matter 15 (2003) 6943–6953.

[68] Z. Zhang, A. Stukowski, H. Urbassek, Interplay of dislocation-based plasticity and phase transformation during si nanoindentation, Comp. Mater. Sci. 119 (2016) 82–89.

[69] Z. Zhang, H. Urbassek, Comparative study of interatomic interaction potentials for describing indentation into Si using molecular dynamics simulation, Appl. Mech. Mater. 869 (2017) 3–8.

[70] J. Sun, L. Cheng, J. Han, A. Ma, L. Fang, Deformation and pop-in events in a silicon crystal: molecular dynamics simulation and experiment, Sci. Rep. 7 (2017) 10282.

[71] J. Han, J. Sun, S. Xu, D. Song, H. Liu, Y. Han, L. Fang, Deformation mechanisms at multiple pop-ins under spherical nanoindentation of (111) Si, Comp. Mater. Sci. 143 (2018) 480–485.

[72] J. Han, Y. Song, W. Tang, C. Wang, L. Fang, H. Zhu, J. Zhao, J. Sun, Reveal the deformation mechanism of (110) silicon from cryogenic temperature to elevated temperature by molecular dynamics simulation, Nanomaterials 9 (2019) 1632.

[73] D. Chrobak, N. Tymiak, A. Beaber, O. Ugurlu, W.W. Gerberich, R. Nowak, Deconfinement leads to changes in the nanoscale plasticity of silicon, Nat. Nanotechnol. 6 (2011) 480–484.

[74] M. Ohbitsu, T. Yokoi, Y. Noda, E. Kamiyama, T. Ushiro, H. Nagakura, K. Sueoka, K. Matsunaga, Atomic structures and stability of finite size extended interstitial defects in silicon, Large-scale molecular simulations with a neural-network potential, Scr. Mater. 214 (2022), 114650.

[75] B.Y. Li, A.C. Li, S. Zhao, M.A. Meyers, Amorphization by mechanical deformation, Mat. Sci. Eng. R 149 (2022), 100673.

[76] H. Chen, V.I. Levitas, L. Xiong, Amorphization induced by 60o shuffle dislocation pileup against different grain boundaries in silicon bicrystal under shear, Acta Mater 158 (2019) 287–295.

[77] H. Chen, V.I. Levitas, L. Xiong, X. Zhang, Stationary dislocation motion at stresses significantly below the Peierls strss: example of shuffle screw and 60o dislocations in silicon, Acta Mater. 206 (2021), 116623.

[78] P. Valentini, W.W. Gerberich, T. Dumitrica, Phase-transition plasticity response in uniaxially compressed silicon nanospheres, Phys. Rev. Lett. 99 (2007), 175701.

[79] A. Dongare, L. Zhigilei, A. Rajendran, B. LaMattina, Interatomic potentials for atomic scale modeling of metal–matrix ceramic particle reinforced nanocomposites, Composites 40 (2009) 461–467.

[80] A.P. Thompson, H.M. Aktulga, R. Berger, D.S. Bolintineanu, W.M. Brown, P. S. Crozier, P.J. Veld, A. Kohlmeyer, S.G. Moore, T.D. Nguyen, R. Shan, M. J. Stevens, J. Tranchida, C. Trott, S.J. Plimpton, LAMMPS - a flexible simulation tool for particle-based materials modeling at the atomic, meso, and continuum scales, Comp. Phys. Comm. 271 (2022), 108171.

[81] P. Branicio, J. Rino, C. Gan, H. Tsuzuki, Interaction potential for indium phosphide: a molecular dynamics and first-principles study of the elastic constants, generalized stacking fault and surface energies, J. Phys. Condens. Matter 21 (2009), 095002.

[82] Atomistica interatomic potentials library. URL https://github.com/Atomistica/atomistica.

[83] L. Hansen, K. Stokbro, B. Lundqvist, K. Jacobsen, D. Deaven, Nature of dislocations in silicon, Phys. Rev. B 75 (1995) 4444–4447.

[84] E. Holmström, A. Kuronen, K. Nordlund, Threshold defect production in silicon determined by density functional theory molecular dynamics simulations, Phys. Rev. B 78 (2008), 045202.

[85] E.R. Batista, J. Heyd, R.G. Hennig, B.P. Uberuaga, R.L. Martin, G.E. Scuseria, C. J. Umrigar, J.W. Wilkins, Comparison of screened hybrid density functional theory to diffusion Monte Carlo in calculations of total energies of silicon phases and defects, Phys. Rev. B 74 (2006), 121102.

[86] A. Stukowski, A visualization and analysis of atomistic simulation data with OVITO–the open visualization tool, Modelling Simul. Mater. Sci. Eng. 18 (2010), 015012.

[87] A. Stukowski, Dislocation analysis tool for atomic simulations, in: W. Andreoni, S. Yip. (Eds.), Handbook of Materials Modelling, Springer, Cham, 2018.

[88] E. Maras, O. Trushin, A. Stukowski, T. Ala-Nissila, H. Jónsson, Global transition path search for dislocation formation in Ge on Si(001), Comp. Phys. Comm. 205 (2016) 13–21.

[89] D. Chrobak, D. Chrobak, R. Nowak, Effect of doping on nanoindentation induced incipient plasticity in InP crystal, AIP Adv. 9 (2019), 125323.

[90] D. Kim, S. Oh, Deformation pathway to high-pressure phases of silicon during nanoindentation, J. Appl. Phys. 104 (2008), 013502.

[91] J. Sun, L. Fang, J. Han, Y. Han, H. Chen, K. Sun, Phase transformations of mono-crystal silicon induced by two-body and three-body abrasion in nanoscale, Comput. Mater. Sci. 82 (2014) 140–150.

[92] J.Z. Hu, L.D. Merkle, C.S. Menoni, L.L. Spain, Crystal data for high-pressure phases of silicon, Phys. Rev. B 34 (1986) 4679.

[93] L. Boyer, E. Kaxiras, J. Feldman, J. Broughton, M. Mehl, New low-energy crystal structure for silicon, Phys. Rev. Lett. 67 (1991) 715–718.

[94] J. Crain, G. Ackland, J. Maclean, R. Piltz, P. Hatton, G. Pawley, Reversible pressure-induced structural transitions between metastable phases of silicon, Phys. Rev. B 50 (1994) 13043–13047.

[95] B.G. Pfrommer, M. Côté, S.G. Louie, M.L. Cohen, Ab initio study of silicon in the R8 phase, Phys. Rev. B 56 (1997) 6662–6668.

[96] J.E. Bradby, J.S. Williams, J. Wong-Leung, M.V. Swain, P. Munroe, Mechanical deformation in silicon by micro-indentation, J. Mater. Res. 16 (2001) 1500–1507.

[97] Y.B. Gerbig, S.J. Stranick, D.J. Morris, M.D. Vaudin, R.F. Cook, Effect of crystallographic orientation on phase transformations during indentation of silicon, J. Mater. Res. 24 (2009) 1172–1183.

[98] L.Q. Huston, A. Lugstein, G. Shen, D.A. Cullen, B. Haberl, J.S. Williams, J. E. Bradby, Synthesis of novel phases in Si nanowires using diamond anvil cells at high pressures and temperatures, Nano Lett. 21 (2021) 1427–1433.